Chapter 1: Introduction

Polymorphism in Organic semiconductors

Organic semiconductors (OSCs) are classified as organic molecules possessing semiconducting properties. OSCs comprise a vast family of semiconductors based on polymers and conjugated molecules. In contrast to inorganic semiconductors, organic semiconductors exhibit unique features, such as mechanical flexibility, solution processability, mixed electronic and ionic conduction, and intense optical absorption and emission [1]. Present and future applications of these OSCs include commercially available organic light emitting displays [2], infrared emitters [3], hybrid organic/inorganic solar cells [4], organic field-effect transistors [5], and so on. Many organic compounds exhibit distinct crystal structures known as polymorphs, and such characteristics are referred to as polymorphism [6]. Since the weak van der Waals forces hold the organic molecules together, they are expected to exhibit many alternative packing with minor differences in structure and energy [7]. In general, the polymorph of a solid exhibits different physical properties such as solubility, hardness, compressibility, density, refractive index, electric conductivity, and melting point [8]. Polymorphism in organic semiconductors can be identified and separated in bulk and thin films [9]. For example, pentacene exhibits two bulk polymorphs in the single crystal form, the high-temperature phase (293 K) or Campbell phase [10] with the d-spacing (001) of 14.4 Å and low-temperature phase (90 K) with the d-spacing (001) of 14.1 Å [11]. Although the polymorphism in bulk crystals is extensively studied, understanding thin film polymorphism is scarce and challenging to control. The approaches employed to tune polymorphs in thin films are by controlling the substrate temperature during deposition, post-deposition thermal annealing, solvent modification or solvent post-deposition treatments, film thickness, template modification, and so on [7]. Thickness-driven phase transformation was observed for pentacene thin films where the orthorhombic phase changes to the triclinic phase through a thin-film phase [12]. Solvent-vapor annealing of thin films of contorted hexabenzocoronene exhibited different out-of-plane orientations with the same crystal structure as the one without annealing [13]. Pentacene molecules generally lie flat on the metal (Au, Cu) substrate surface [14,15], while the edge-on configuration is also observed under specific conditions [16]. In the case of these organic semiconductors, a slight change in the packing of the molecules lead to orders of magnitude difference in their electronic and optical properties [17]. For example, rubrene exhibits various polymorphs corresponding to monoclinic [18], triclinic [19], and orthorhombic [20] crystal structures. The triclinic and

monoclinic forms of rubrene manifest high singlet fission efficiency than the orthorhombic form [21]. Here, the crystal packing in the polymorphs of rubrene induced different coupling between the neighboring molecules, which led to the modification of the fundamental band gap and band dispersion. Tetracene polymorphs were formed by cooling the thermally evaporated films on glass substrates to room temperature (polymorph Tc I) and liquid nitrogen temperature of 93 K (polymorph Tc II) [22]. Here the singlet fission was faster in polymorph Tc II compared to polymorph Tc I, but, unlike in Tc I polymorph, the rate of singlet fission was found to be independent of the crystallite size in Tc II polymorph. Hence polymorphism eliminates the requirement of chemical modification of the parent compound, and also proves to be a valuable investigating tool to study the effects of solid-state packing on the various physical properties of the material.

Polymorphism in metallophthalocyanines

Among the organic semiconductors, metal phthalocyanines (MPcs) are a prominent class of molecules studied extensively as active materials in organic electronics [23]. MPcs are macrocyclic compounds in which 70 different metals [24] and also non-metals can be incorporated, opening the door to a variety of applications in organic photovoltaics, dyes, and pigments [25], imaging agents [26], and catalysts [27]. They consist of four isoindole subunits with 18 π-electrons analogous to naturally occurring porphyrins, such as hemoglobin, chlorophyll, and so on [28]. This electronic delocalization allows MPcs to exhibit intense absorption bands in the near-infrared region with high extinction coefficients (~ 10^5 $M^{-1}cm^{-1}$), and also exhibit high fluorescence quantum yields [29]. The occurrence of phthalocyanines as various polymorphs subjects to a wide variety of applications with unique physical properties. Titanyl phthalocyanine exists as four polymorphs: a monoclinic phase I [4], phase C [5], a triclinic phase II [4], and another monoclinic phase Y [6]. The organic solar cell with titanyl phthalocyanine as the donor layer showed a strong dependence of photocurrent yield and solar cell efficiency on the polymorphs of titanyl phthalocyanine [30]. Organic vapor phase deposition of fluorinated copper phthalocyanine gave rise to a new polymorph with nanowire-like morphology [31]. The photo-detector based on these nanowires showed a fast response with a response time of around 448 ms under the visible (589 and 628 nm) and NIR light illumination (850 nm and 940 nm).

This thesis consists of five chapters. The fundamentals of polymorphism and its importance in organic semiconductors are discussed in Chapter 1. Chapter 2 discusses the deposition and fabrication techniques of phthalocyanine films and devices and their characterization

techniques. Chapter 3 discusses the self-affine growth of the polymorph of Nickel octabutoxy phthalocyanine and its application as a detector in the UV regime. Chapter 4 discusses the optical properties of the as-deposited and annealed thin films of Nickel octabutoxy phthalocyanine. Chapter 5 discusses the polymorphs of Copper and Zinc octakis-octyloxy phthalocyanine and their mixture exhibiting different photoluminescence features. Chapter 6 discusses the summary and future scope of the work.

Chapter 2: Experimental methodology

Surface manometry

The surface manometry technique is used to study the phase transitions of the compound at the air-water (A-W) interface [32]. Classical systems like fatty-acids and lipids form such monolayers. An amphiphile consists of two different parts, referred to as head and tail groups. The head part is the hydrophilic group, and the tail part is the hydrophobic group. If the molecule has enough hydrophobic parts, then the molecule is insoluble and such molecules form a two-dimensional isolated system at the A-W interface. Such monomolecular insoluble films formed at the A-W interface are known as Langmuir monolayers or Langmuir films. The compression of these monolayers at the A-W interface induces transitions to various phases of the compound [32]. Monitoring the surface pressure and area of the monolayer during the compression establishes surface pressure-area per molecule (π–A_m) isotherm that depicts the phases of the monolayer. The surface manometry of the metal-phthalocyanine (MPc) was carried out at the A-W interface using a Langmuir-Blodgett (LB) trough (KSV NIMA). Ultra-pure water of resistivity 18.2 MΩ cm (Millipore) was used as a subphase in the LB trough. The MPc was dissolved in chloroform (~ 5 x 10^{-5} M) to form a clear solution. This solution was spread dropwise using a micro-syringe (Hamilton) at the A-W interface of the LB trough. The pressure sensor was used to measure the surface-pressure through a Wilhelmy plate attached. After equilibrating for 30 min for the evaporation of the solvent, the floating film was compressed at a rate of 7 cm^2 min^{-1} using Teflon barriers and simultaneously, the π–A_m isotherm was recorded.

Brewster angle microscopy

Brewster Angle Microscopy (BAM) is a non-invasive optical technique that enables the real-time observation of the textures of Langmuir monolayers [33]. The textures of the phthalocyanine at the A-W interface are investigated using BAM in reflection geometry.

Here, a laser (532 nm) beam in transverse magnetically polarized is incident at Brewster angle (53.1^{o}) of water. The presence of a monolayer generates some contrast that otherwise appears dark. BAM images of MPCs at the A-W interface were obtained using a single wavelength imaging ellipsometer (Accurion) with a lateral resolution of 2 μm.

Langmuir-Blodgett deposition

MPc is dissolved in chloroform and spread dropwise onto the LB trough at the A-W interface to form a Langmuir monolayer. Post spreading, the monolayer confined between two barriers (Teflon) is compressed symmetrically at a rate of 7 $cm^2\ min^{-1}$ using an LB trough. Then the π–A_m isotherm for MPc is monitored, and the desired target pressure is obtained under ambient conditions. At this target pressure, multilayers of MPc are transferred onto silicon/glass/quartz substrates using a dipper attached to the LB trough. The number of layers to be deposited and the speed of the downward and upward movement of the substrate during deposition was controlled using the software (KSV NIMA). The efficacy of the transfer is inferred through the transfer ratio (ratio of decrease in monolayer area and area of the substrate).

Stylus profilometry

Stylus profilometry is a technique that uses a physically moving probe along the surface of the thin-film to detect the surface and thereby acquire the surface height. This method requires the presence of a step between the substrate surface and the thin-film surface. The thickness of the MPc thin films deposited using the LB method was measured using the Stylus profilometer (DektakXT, Bruker).

Grazing incidence X-ray diffraction

The structural information of MPc thin films is gleaned using grazing incidence X-ray diffraction (GIXD) operated under ambient conditions. Here the X-ray diffractometer (Smartlab, Rigaku) is set in parallel beam geometry. Cu K_α radiation (wavelength, λ=1.541 Å) is used and the maximum current and tube voltage was set at 30 mA and 40 kV, respectively. The glancing angle is set at 0.3° and the angle is scanned from 2° to 15° in steps of 0.01˚ at a rate of 1˚/min.

Atomic force microscopy

The atomic force microscope (Agilent 5500) operated in the tapping mode was used to

acquire the topographic images of the MPc thin films. For these measurements, a silicon cantilever tip with its resonance frequency at 302 kHz (force constant = 46 N/m) is used. High-resolution topography images (512 × 512 pixels) with a scan size of 3 × 3 μm^2 were acquired. These images were analyzed using Gwyddion software. Three different regions of interest of these films are sampled under ambient conditions, and an average of them is reported. From the topography images, the height profiles were extracted and analyzed.

Spectroscopic ellipsometry

The ellipsometry measurements were performed using the spectroscopic ellipsometer (Alpha-SE, J. A. Woolam. Co). Here the spectroscopic ellipsometer operates in a rotating compensator configuration. The ellipsometer measures the change in the state of polarization as the light reflects from the sample. Here the linearly polarized light with transverse magnetic (electric field parallel to the plane of incidence) and transverse electric (electric field perpendicular to the plane of incidence) components was incident onto the sample. The change in polarization of the reflected light is measured in terms of reflectance ratio as, $\rho = \frac{R_p}{R_s}$, where R_p and R_s are the reflectance of the p and s polarized light. In ellipsometry, we measure the parameters ψ and Δ, given by $\rho = \frac{R_p}{R_s} = \tan\psi \exp(i\Delta)$ where $\tan\psi = \left|\frac{R_p}{R_s}\right|$ and $\Delta = \delta_{rp} - \delta_{rs}$ represents the amplitude ratio and phase difference between p and s polarized light respectively. The measurements were performed in the wavelength range 380-900 nm, at different incident angles (65^o, 70^o, and 75^o). CompleteEase software was used to fit the experimental data and extract the optical functions.

Ultraviolet-visible near-infrared absorbance spectroscopy

The UV-visible absorbance of MPc LB films deposited on to quartz substrate was carried out using an ultraviolet-visible and near-infrared spectrophotometer (AvaSpec-ULS2048XL-RS-SPU2, Avantes). Here the deuterium–halogen light source was used to acquire the absorption spectra at normal incidence from 200 to 1100 nm.

Photoluminescence spectroscopy

Steady state photoluminescence spectra for the MPc LB films were investigated using the Fluorolog 3 (FL3-21, HORIBA Jobin Yvon Ltd) spectrofluorometer. The excitation wavelengths 280, 300, and 320 nm were used with the excitation and emission slit size of 2 nm.

DC magnetron sputtering

The glass substrates were cleaned and masked (width 100 μm) for the fabrication of in-plane gap electrodes. Then titanium/gold film (~10/100 nm thick) was sputtered in sequence using a tabletop sputtering unit (BT 300, Hind High Vacuum, India) to obtain the required gap electrodes.

Photocurrent measurements

The electrical characterization of MPc thin film (thickness ~180 nm) was carried out using the source meter (2614b, Keithley Instruments). The J-V measurements of the MPc thin films were carried out using the source meter in the dark and with the UV (365 nm) illumination at different power densities (PM100D, Thorlabs). The photocurrent response of the MPc thin films under UV illumination was also monitored with time at fixed bias voltage and different power densities.

Chapter 3: UV photodetector based on self-affine Langmuir-Blodgett film of nickel octabutoxy phthalocyanine doped with stearic acid

The control of thin-film deposition, surface morphology and the nature of polymorph plays a vital role in dictating the efficiency of electronic devices and hence understanding the growth dynamics of these materials is highly desirable [34]. When compared to thin films of inorganic semiconductors, the growth dynamics of organic phthalocyanine thin films are more complex because of weak intermolecular interaction resulting in smaller sublimation enthalpies and low barriers for the diffusion molecules [35]. Several factors can potentially affect the growth of organic thin films such as the surface and interfacial energy of the film with the substrate, diffusion of molecules at the surface, step-edge barriers and so on [36]. Scaling theory is applied to study the growth behaviour of organic thin films by many researchers [37–39]. Surfaces that exhibit equal scaling in the lateral directions on the surface but not in the orthogonal direction are referred to as self-affine surfaces. Thus, it differs from the self-similar surface, which demands equal scaling in all the three directions. Such self-affine surfaces are reported for several thin films of organic semiconductors, including phthalocyanines [37,40]. Further useful information on the growth processes leading to rapid roughening [41], Ehrlich-Schwöbel barrier [42] and Stranski-Krastanov

growth mode [43], were gleaned by studying the scaling exponents. The surface topography images obtained using atomic force microscopy (AFM) measurements along with height difference correlation function (HDCF) analysis provide more insights into the growth process and can be described using some simple scaling laws. The interplay between diffusion type and step-edge barrier of growth mechanisms leading to fractal-mound growth is reported for pentacene thin films grown on SiO_2 substrates [39]. The sulfonated copper phthalocyanine (CuTsPc) when drop casted onto glass and quartz substrates, exhibited multifractal nature on the surface [44]. This study provided a greater insight into the quality control of surface roughness. Kim et al. reported the dependency of crystallinity on the dynamic scaling behaviour of TioPc and ZnPc thin films [45]. Here TioPc films do not show anomalous scaling behaviour which is generally observed in crystalline molecular thin films, revealing the amorphous character of the films and subsequent small step edge barriers. These studies provided useful insights on the factors affecting the growth dynamics and paved the way for better device performance.

Here, we focus on the aspect of growth dynamics first, followed by the photodetecting behaviour in the UV region for Langmuir-Blodgett (LB) films of $NiPc(OBu)_8$ doped with stearic acid at interfaces. The chemical structure of $NiPc(OBu)_8$ and stearic acid is shown in Figure 1a.

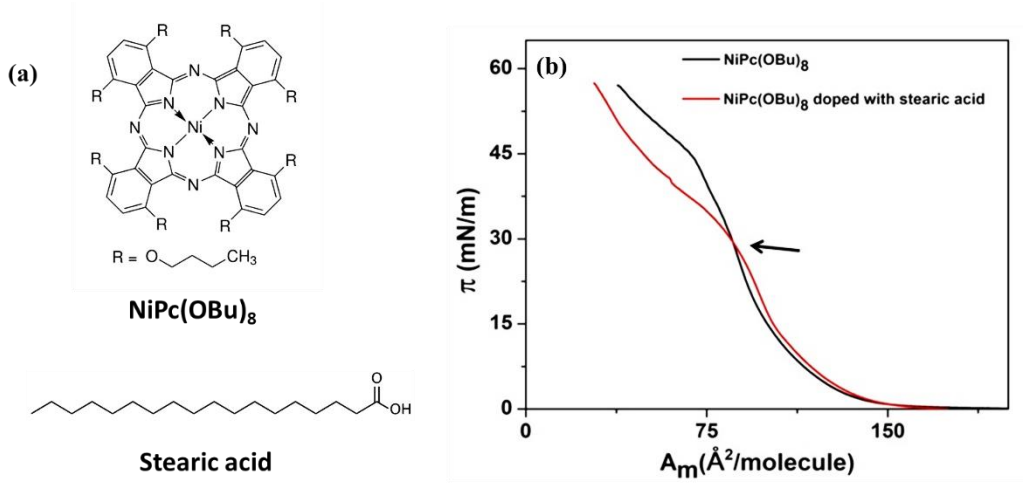

Figure 1: (a) **C**hemical structure of $NiPc(OBu)_8$ and stearic acid. (b) Surface pressure-area per molecule **(**π-A_m) isotherms of $NiPc(OBu)_8$ and $NiPc(OBu)_8$ doped with stearic acid at the air-water interface. The arrow mark shows the target surface pressure (25 mN/m) at which the film is transferred.

Surface manometry studies on $NiPc(OBu)_8$ and $NiPc(OBu)_8$ doped with stearic acid were carried out at air-water interface at 293 K. π-A_m isotherms of $NiPc(OBu)_8$ and $NiPc(OBu)_8$

doped with stearic acid at the air-water interface is shown in Figure 1b. The isotherm steeply rises at 150 Å^2/molecule for both cases and exhibits a similar trend until 80 Å^2/molecule. Below 80 Å^2/molecule, the gradual collapse behaviour of NiPc(OBu)$_8$ doped with stearic acid is seen. The lift-off area remains unaltered at 150 Å^2/molecule.

Grazing incidence X-ray diffraction studies were carried out for the multilayers of NiPc(OBu)$_8$ doped with stearic acid of different thicknesses under ambient conditions (Figure 2). A Bragg peak at 2θ = 4.15° (d = 21.3 Å) is observed for these multilayers ascertaining the crystalline nature of the thin film polymorph. With the increase in thickness, the Bragg peak becomes sharper and narrow (decreasing FWHM). The crystallite size was evaluated using Scherrer's formula, $d = 0.9\lambda/(FWHM * cos\theta)$, where FWHM is the full width at half-maximum of the Bragg peak, λ is the wavelength of the X-ray and θ is the Bragg angle.

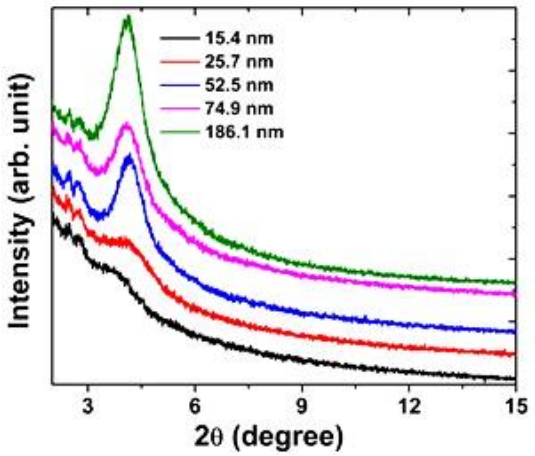

Figure 2: Grazing incidence X-ray diffraction pattern of LB films of NiPc(OBu)$_8$ doped with stearic acid on Si substrate.

The crystallize size was found to saturate beyond a thickness of 75 nm. Figure 3 shows the surface topography of NiPc(OBu)$_8$ films doped with stearic acid obtained using an atomic force microscope (AFM). It is evident from these images that the granular structures persist for the LB films of different thicknesses. The grain coverage and also its size is found to increase with a thickness which is consistent with the inference drawn from the X-ray studies. From the topography images, the height profiles were extracted. Figure 4 shows the variation of the height-height correlation function, g(R) with thickness extracted from topography images for LB films of NiPc(OBu)$_8$ doped with stearic acid. The roughness exponent (α), surface roughness (σ) and the correlation length (ξ) were obtained by fitting them to equation,

$$g(R) = 2\sigma^2[1 - exp(-(R/\xi)^{2\alpha})] \qquad (1)$$

where R is the distance of separation between two points acquired from the AFM image, σ is

the RMS roughness of the surface, ξ is the correlation length of the surface, and α is referred to as roughness (or Hurst) exponent. The parameters ξ and σ are related to film thickness, t by $\xi \propto t^{1/z}$ and $\sigma \propto t^{\beta}$. α, β and dynamic exponent, z, obey the scaling law, $z = \frac{\alpha}{\beta}$. The scaling exponents governing the growth dynamics is obtained through linear fits as, β = 0.22 ± 0.1 and 1/z = 0.17 ± 0.01, respectively for the LB films. We find that the local exponent α increases with the thickness and tends to saturate at 0.92 (lesser than 1). A similar trend of α is also reported in the literature [41]. The variation of the surface roughness, σ with correlation length, ξ, which yield the growth exponent, γ = 1.40 ± 0.25. Further, this can be compared with the ratio of β and 1/z which is found to be 1.29. This value is comparable with the fitted γ within the experimental error. The exponent, γ predicts the competition

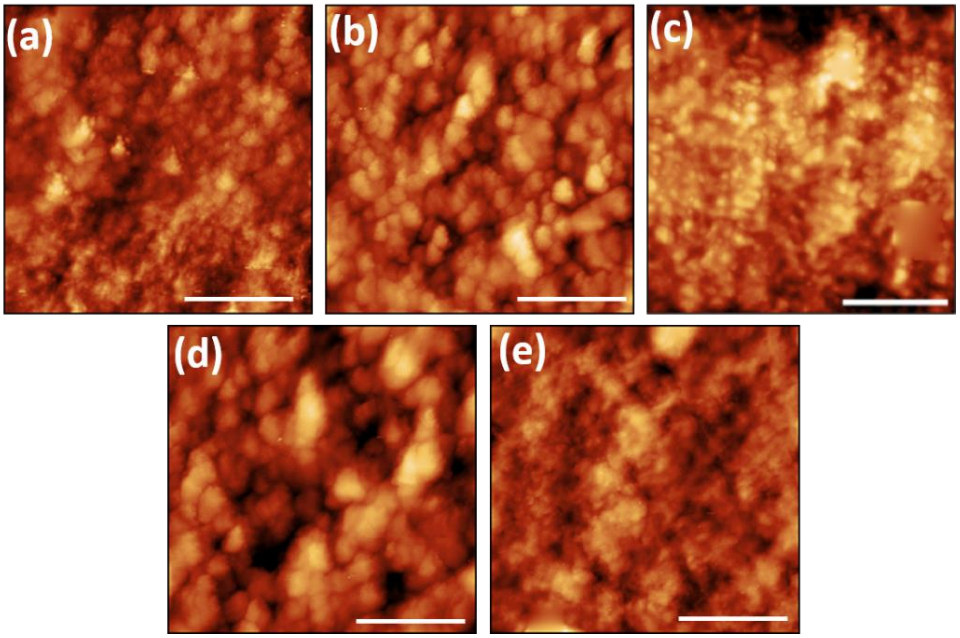

Figure 3: Surface topographies of LB films of NiPc(OBu)$_8$ doped with stearic acid of different thicknesses (a) 15.4 nm (b) 25.7 nm (c) 52.5 nm (d) 74.9 nm and (e) 186.1 nm obtained using an atomic force microscope. Scale bar represents 1 μm.

between the lateral and vertical growth. In our case, we observe γ > 1 indicating faster vertical growth. Zhang et al. have reported a layer dependence growth of di-indenoperylene films on SiO_2 with E-S barrier [46]. They have related the initial stage of growth to variation of interlayer transport with thickness and molecular reorientations. In the LB method of deposition, the preformed film at the air-water interface is sequentially transferred to the substrate under ambient conditions. As no external stimulus (substrate temperature) is involved during film growth, the roughening mainly competes with the adsorption energy of the molecules on the surface and its surface energy which can be attributed to the kinetic

roughening [47].

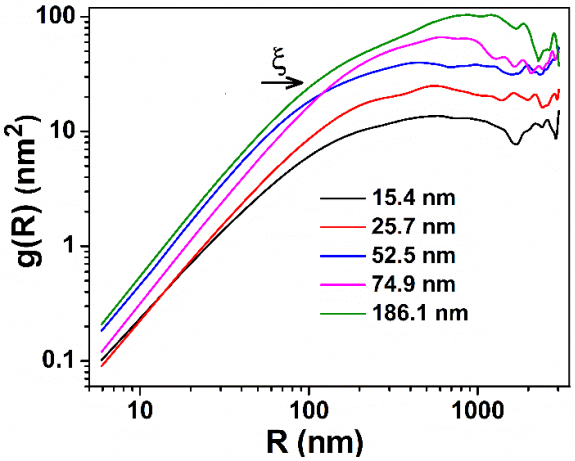

Figure 4: Variation of height-height correlation function (g(R)) with distance (R) for LB films of $NiPc(OBu)_8$ doped with stearic acid of different thicknesses.

The UV-near infrared absorbance studies for the LB films of $NiPc(OBu)_8$ doped with stearic acid show sharp bands at higher wavelength corresponding to an electronic transition due to the Q band (around ~760 nm) followed by Soret or B band (around ~317 nm) at a lower wavelength. The Q and B bands are attributed to the transition of the electron from the ground state to the first excited state ($S_0 \rightarrow S_1$) and the transition of an electron from the ground state to the second excited state, respectively. Compared to the absorbance spectra of solution, the LB film of $NiPc(OBu)_8$ doped with stearic acid shows a bathochromic shift (20 nm) in the Q band (around ~760 nm). This shift in the band can be due to the formation of J-aggregates in LB film [48]. The electrical characterization of the multilayer film of $NiPc(OBu)_8$ is studied under dark and UV illumination in reflection geometry. The current density-voltage (J–V) curves for the LB film of $NiPc(OBu)_8$ doped with stearic acid under dark and upon UV (365 nm) illumination at a power density of 166 $mWcm^{-2}$ show non-linear behaviour of J–V asymmetric to the origin. This is due to the Schottky barrier contact formed between the gold and $NiPc(OBu)_8$ on either side of the LB film. The highest dark current density observed is around 0.44 μAcm^{-2} at 10 V. Upon UV illumination, the current density rises to 1.5 μAcm^{-2} for 10 V bias. With increase in power density, a concomitant increase in photocurrent is observed.

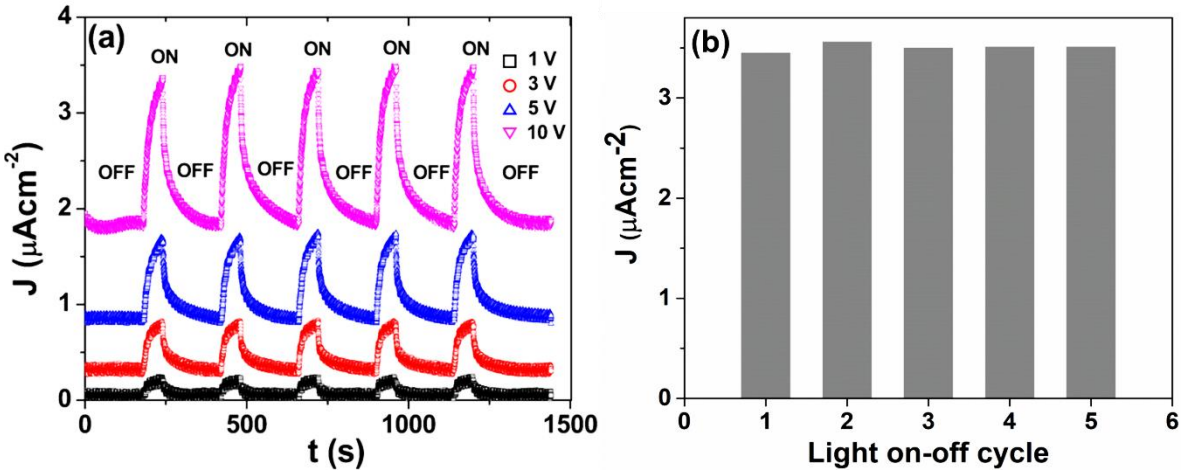

Figure 5: (a) Variation of photocurrent density (J) with time (t) for the LB film of $NiPc(OBu)_8$ doped with stearic acid with UV illumination (365 nm) of power density of 166 $mWcm^{-2}$ for different bias voltage. (b) Peak photocurrent obtained for different light on-off cycles at a fixed bias of 5 V.

The evolution of photocurrent with time is measured under UV illumination at different bias voltages for an LB film of $NiPc(OBu)_8$ doped with stearic acid is shown in Figure 5a. When the illumination is turned on, the photocurrent increases to 3.5 μAcm^{-2}. The photocurrent returns close to its original value when the illumination is turned off. The detector shows good stability when repeated for five light on-off cycles (Figure 5b). At 5 V, the rise (10 – 90% of the response) and decay (90 – 10% of the response) time is found to be 39.5 s and 74.8 s, respectively at 166 $mWcm^{-2}$. Luc et al. reported that ZnPc based photodetector exhibited good photosensitive performance with photocurrent density around 0.7 Acm^{-2} (265 nm, 730 μWcm^{-2}) and fast rise and decay time of 0.142 s and 0.186 s [49]. Compared to this our device shows a slower photocurrent response with response time up to a few tens of seconds. We suggest that the slower response of the photocurrent may be due to a mismatch in the illumination with respect to its peak absorbance, low mobility of carriers and disordered molecular arrangement [50]. With the decrease in power density, the rise and decay times marginally increase. The time-dependent photocurrent response obtained for different power densities at a fixed bias of 5 V was found to increase with power density. The responsivity (R) and external quantum efficiency (EQE) are calculated using the equations, $R = \frac{I_{ph}}{P}$ and $EQE = R\frac{hc}{q\lambda}$, respectively [51]. Here I_{ph} is the photocurrent, P is power of incident light, h is the Planck's constant, c is the velocity of light in vacuum, q is the electron charge and λ is the wavelength of incident light. The responsivity (R) with power

density P_d varied from 0.2 to 0.9 μAW^{-1}. The device showed a maximum EQE of about 0.0003% for a power density of 166 μWcm^{-2}.

Chapter 4: Optical studies on Langmuir-Blodgett film of nickel octabutoxy phthalocyanine doped with stearic acid

Phthalocyanines (Pcs) are macrocyclic compounds used as organic semiconductors characterized with planarity, symmetry and electron delocalization [52]. Such organic semiconductors have shown wide spread usage in thin-film transistors [53], and optoelectronic devices [54], and organic photovoltaics [55]. Among them, the existence of Pcs in various crystal forms known as polymorphs, extended π conjugation of electrons and excellent thermal and chemical stability render phthalocyanine stand unique [56]. In general, a polymorph of a solid exhibits different physical properties such as solubility, hardness, compressibility, density, refractive index, electric conductivity and melting point [8]. The metal-free phthalocyanine (Pc) crystallize into a variety of polymorphs [57]. The two important phases are identified as α and β. Here both α and β phases exhibit herringbone structure stacked along b-axis but are differentiated by the angle between the plane of the molecule and the stacking axis. The α phase is obtained by growth at room temperature on weakly interacting substrates like glass [58]. High-temperature growth or post- growth annealing of a thin film leads to the formation of β films [59]. The thin films grown at high substrate temperature and the films annealed post deposition can also be differentiated structurally. These two structures have recently been characterized by powder X-ray diffraction and are labelled β_1 [60] and β_2 [57] respectively for the metal-free phthalocyanine thin films. A lot of research has been carried out to understand the control of these polymorphs through the growth dynamics [40], crystallinity [61], control of morphology [62], and molecular orientation [63]. These factors are said to affect the device parameters and excitonic properties [64]. Since the nature of polymorph plays a vital role in dictating the efficiency of electronic devices, identifying and understanding the control of these polymorphs is highly desirable.

There has been a recent focus in the photoluminescence and electroluminescence characteristics of metallo-phthalocyanines (MPc's) leading to interesting optoelectronic devices [65]. Silicon phthalocyanine showed emission in the visible region that was attributed to recombination of charge carriers between conduction band and valence band [66]. The π- π conjugation in Pcs also lead to excellent photochemical stability and light

harvesting capability [67]. The photoluminescence in the MPc's also depend on the nature of the polymorph [68]. Dual emission lead by the tuning of crystallinity of polymorphs was reported for zinc phthalocyanine (ZnPc) upon excitation of 685 nm [69]. Here the α and β phases of ZnPc films showed distinct luminescent behavior at 930 and 780 nm, attributed to excimer and Frenkel emissions respectively. Contrary to the unsubstituted Pcs, that have poor solubility and high aggregation tendency, substituted Pcs exhibit higher solubility [55] and assist in solution processability. The thin films of substituted Pcs lead to various applications such as organic solar cells[70], organic light emitting diodes [71], organic field emission diodes [72] and so on.

The absorption properties of the MPc's are extensively studied and their spectra is assigned to the electron orbital transitions [73]. The schematic of the as-deposited (298 K) and annealed (423 K) LB films of NiPc(OBu)8 doped with stearic acid is shown in Figure 6a. Generally five optical transitions corresponding to Q, B, N, L and C bands are identified for the MPc's corresponding to wavelengths 620, 345, 280, 248 and 210 nm respectively [16]. Figure 6b shows the UV visible-near infrared absorbance spectra in the energy ranging between 1.2 and 6.2 eV for the as-deposited and annealed LB films of NiPc(OBu)8 doped with stearic acid deposited on to quartz substrates. The absorption spectra were deconvoluted using the Gaussian function and the peak parameters were extracted. The sharp bands of the absorbance spectra at higher wavelength seen for both cases correspond to an electronic transition due to the Q band (around ~ 750 nm) followed by Soret or B band (around ~320 nm) at a lower wavelength.

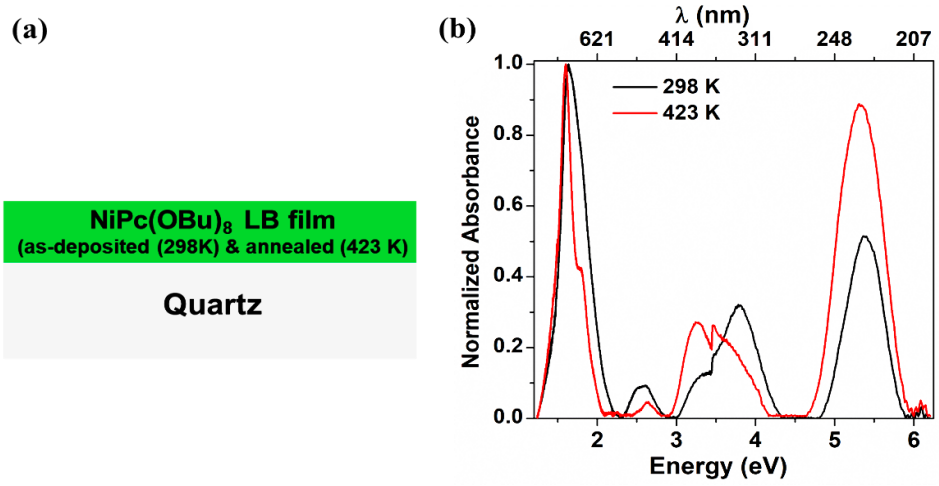

Figure 6: (a) Schematic of the LB films. (b) UV-Visible absorbance spectra of the as-deposited (298 K) and annealed (423 K) LB films of $NiPc(OBu)_8$ doped with stearic acid.

The Q and B bands are attributed to the transition of the electron from the ground state to the first excited state (S0 → S1) and to the second excited state, respectively. For the as-deposited case, the intense peak at lower wavelength is observed to be around ~231 nm. We also observe other low intense absorption peaks at 346, 384 and 483 nm. Here the prominent peak in the Q band is observed at ~710 nm is accompanied by the other low intense peaks around 770 and 816 nm. These observations are in agreement with the literature [73]. Compared to the absorbance spectra of $NiPc(OBu)_8$ in solution [74], the as-deposited LB films of $NiPc(OBu)_8$ doped with stearic acid shows a bathochromic shift (~20 nm) in the Q band attributed to the formation of J-aggregates [48]. For the annealed case, we find the intense peak at lower wavelength to be around ~ 234 nm accompanied by other low intense peaks at 348, 386 and 472 nm. Here the prominent peak in the Q band is observed at ~ 773 nm with other low intense peaks occurring around ~ 686 and 796 nm. The change in the prominent peak positions of the Q band for the as-deposited (~ 710 nm) and annealed (~ 774 nm) LB films signifies the polymorphic transition upon thermal annealing [22]. Such relative change in the peak position of high intense peak in the Q band confirmed the transformation from α to β polymorph of copper phthalocyanine thin films [76]. Although MPc's show only minor changes in optical bandgap upon varying the central metal atom, their photoresponses seems to be different [77]. This suggests the involvement of localized 'd' and delocalized $\pi-\pi^*$ states contributing to low energy. The electronic structure studied for the nickel phthalocyanine (NiPc) in gas phase using the density functional theory with optimally tuned range-separated hybrid functionals reported the optical band-gap of 2.098 eV. The energy gap of the $NiPc(OBu)_8$ determined through absorbance spectra of the $NiPc(OBu)_8$ solution was reported to be 1.6 eV [78]. This shift in energy gap of $NiPc(OBu)_8$ compared to NiPc, is attributed to the presence of peripheral butoxy groups [74].

We have carried out the photoluminescence studies of the solution, as-deposited and annealed LB films of NiPc(OBu)8 doped with stearic acid. The normalized photoluminescence spectra of the solution of NiPc(OBu)8 doped with stearic acid is shown in Figure 7a. The spectra was collected for the excitation wavelength of 320 nm. Prominent photoluminescence (PL) peak was observed around ~ 440 nm along with other peaks appearing around 380, 420 and 450 nm. Interestingly, we find both the as-deposited and annealed LB films exhibit luminescence. Figure 7b shows the normalized photoluminescence of the as-deposited and annealed thin films of $NiPc(OBu)_8$ doped with stearic acid at an excitation wavelength of 320 nm. Scrutinizing the PL peak parameters of the as-deposited LB film yields the characteristic

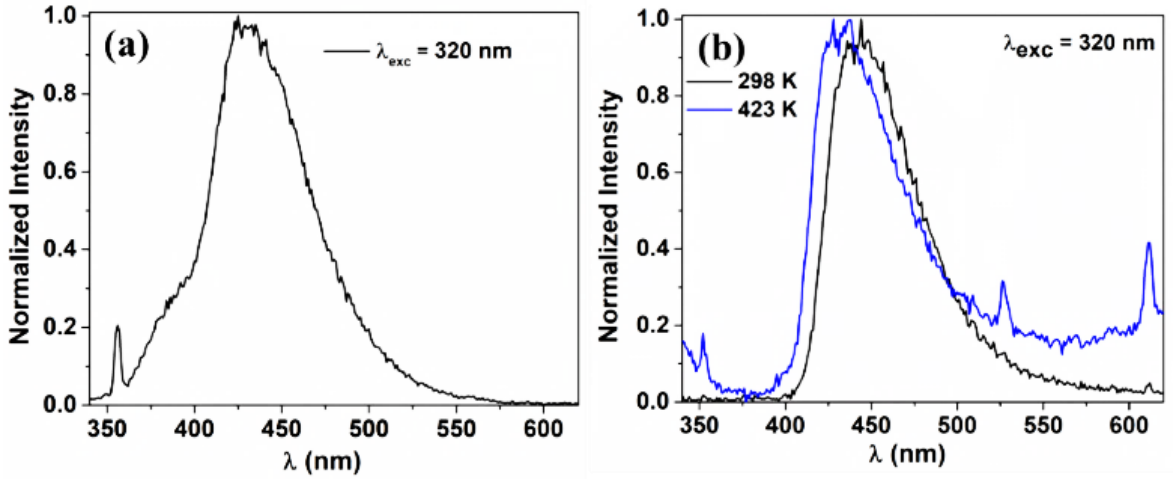

Figure 7: Normalized photoluminescence spectra of the (a) solution and (b) as-deposited (black) and annealed (blue) LB films of $NiPc(OBu)_8$ doped with stearic acid at an excitation wavelength, λ_{exc} = 320 nm.

peaks around 428, 445, 465 and 490 nm. Upon analysis of the PL spectra of annealed LB films, a clear blue shift (~ 420, 435, 450 and 480 nm) is observed in PL peak position compared to that of as-deposited case (~ 428, 445, 465 and 490 nm). We attribute this behavior in the shift to the polymorphic transformation. Copper phthalocyanine also showed a blue shift in the emission spectrum of β-phase compared to the α-phase [79]. In addition to this, unlike as-deposited case, annealed film yield a new peak around 530 nm. The PL peaks observed for solution and LB films of $NiPc(OBu)_8$ doped with stearic acid may be attributed to the S_2 to S_0 transitions [80,81]. The change in the molecular arrangement and orientation in the thin films can modify the peak parameters of the PL spectra for different polymorphs [60,82]. For both the as-deposited and annealed cases, from the absorption spectra we can identify five transitions in the wavelength range 380-900 nm. For different MPcs, although the peak position corresponding to these transitions are very close, the broadening and the strengths of oscillators vary significantly[83].

Generally, in the case of MPcs, the ψ and Δ measured through spectroscopic ellipsometry (SE) were fitted using the Gaussian and Lorentz models [84]. Some studies have also used Lorentz model [85–87]. But in few cases, some of the peaks were found to fit to Lorentzian and some to the Gaussian models. The Lorentzian model failed to obtain good agreement with the SE measurements of 3,4,9,10-perylenetetracarboxylic dianhydride (PTCDA) [88]. This is because spectral line shape in the Lorentzian model has wide edges, leading to higher absorption than the actual one. By replacing the broadening term, Γ, with the energy dependent broadening, Γ', a better agreement was observed for the SE studies on PTCDA

[85]. This model is referred as the modified Lorentz model (MLM). The MLM model have shown better agreement with the SE data of many organic thin films, particularly with phthalocyanine films [83,88]. Here we have fitted the experimentally obtained ellipsometric parameters ψ and Δ using the Modified Lorentz model (MLM). The pseudo-dielectric function, ε, calculated from the SE measurements (ψ, Δ) is given by [89],

$$\varepsilon(\omega) = sin^2\theta_i \left[1 + tan^2\theta_i \left(\frac{1-\rho}{1+\rho}\right)^2\right] \qquad (2)$$

where, θ_i, is the angle of incidence and $\rho = \tan\psi \exp(i\Delta)$, is the complex reflectance ratio. In this MLM model, the pseudo-dielectric function (Equation 2) was fitted using the dielectric function (Equation 3) obtained from the MLM with four oscillators given by [90],

$$\varepsilon(\omega) = \varepsilon_\infty + \sum_j \frac{F_j}{\omega_j^2 - \omega^2 - i\Gamma_j'\omega} \qquad (3)$$

$$\Gamma_j'(\omega) = \Gamma_j(\omega)\exp\left[-a_j\left(\frac{\omega-\omega_j}{\Gamma_j}\right)^2\right]$$

Where $\varepsilon(\omega)$ represents the complex dielectric function (or modified Lorentz oscillator) as a function of photon energy, ω in eV, j is the number of oscillators, ω_j is peak frequency of oscillator in eV, F_j and Γ_j are the strength and broadening of the j_{th} oscillator respectively. Here ω_j was fed into the model (Equation 3) and F_j *(eV)*, Γ_j *(eV)*, and ε_∞ were fitted along with the thickness. We have ignored the surface roughness as it was found to be quite low (~ 5 nm). As the thin films are of thickness < 100 nm, we have used an isotropic model [91] and have ignored the optical anisotropy.

Parameter	ω (eV)	F (eV²)	Γ (eV)	a	ε_∞
osc. 1	1.63	0.12	0.14	0.06	2.36
osc. 2	1.72	0.82	1.11	1.00	
osc. 3	1.86	0.16	0.29	0.41	
osc. 4	2.62	0.02	0.27	0.02	

Table 1: The model parameters for MLM obtained for the as-deposited (298 K) LB films of $NiPc(OBu)_8$ doped with stearic acid.

Parameter	ω (eV)	F (eV²)	Γ (eV)	a	ε_∞
osc. 1	1.63	0.12	0.12	1.00	2.32
osc. 2	1.77	0.62	0.39	1.00	
osc. 3	1.82	0.01	3.00	0.00	
osc. 4	2.63	0.31	0.82	0.00	

Table 2: The model parameters for MLM obtained for the annealed (423 K) LB films of $NiPc(OBu)_8$ doped with stearic acid.

The measured data were fitted and assessed by the root mean squared error (MSE) given by [92],

$$MSE = \sqrt{\frac{1}{3n-m}\sum_{i=1}^{n}\left[\left(\frac{N_{E_i}-N_{G_i}}{0.001}\right)^2+\left(\frac{C_{E_i}-C_{G_i}}{0.001}\right)^2+\left(\frac{S_{E_i}-S_{G_i}}{0.001}\right)^2\right]} \qquad (4)$$

Where *'n'* is the number of wavelengths, *'m'* is the number of fit parameters, $N = \cos(2\psi)$, $C = \sin(2\psi)\cos(\Delta)$, $S = \sin(2\psi)\sin(\Delta)$, E_i is the experimentally measured data and G_i is the fitted data. Lower *MSE* values indicate the goodness of the fitted data. The fitted thickness was found to be 65 nm for the as-deposited and 74 nm for the annealed LB films. The model parameters extracted for the as-deposited and annealed LB films are listed in Table 1 and Table 2, respectively. From the fitted values of the broadening factor, α, in MLM, we find that not all the peaks are Lorentzian. The Lorentz model results from homogeneous broadening mechanisms in which all molecules have the same transition energy and relaxation processes. Gaussian bands, on the other hand, arise from an inhomogeneous broadening mechanism [93]. This suggests that some of the individual transitions may be Lorentzian, while the overall spectra may not necessarily be Lorentzian [83]. The MSE of the fitting was found to be 7 and 3 for the as-deposited and annealed case. The MLM model shows good agreement with the experimental results for the as-deposited and annealed LB films of $NiPc(OBu)_8$ doped with stearic acid. The optical constants extracted for the as-deposited and annealed films show a distinct behavior (Figure 8) which is attributed to different polymorphs of $NiPc(OBu)_8$.

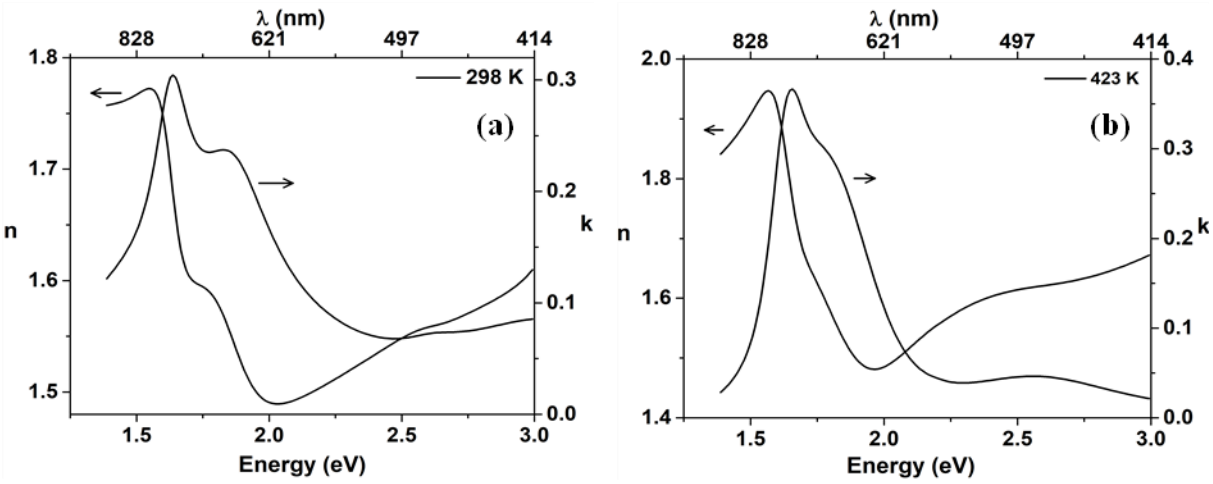

Figure 8: Variation of refractive index, n, (a) and (b) extinction coefficient, k, with energy for the as-deposited (298 K) and annealed (423 K) LB films of $NiPc(OBu)_8$ doped with stearic acid.

Chapter 5: Photoluminescence in annealed thin-film polymorphs of copper and zinc octakis-octyloxy phthalocyanine and their mixture

Small-molecule organic semiconductors act as a model class of compounds for organic–organic heterostructures. Among these small-molecule organic semiconductors, phthalocyanines have led to a large variety of applications in organic electronics and are of high importance. Some of the phthalocyanine derivatives are known to display liquid crystalline phases, and these are of utmost technological importance [94]. The latter type is widely used in organic thin-film devices for improvement in conductivity or efficient charge carrier separation [95]. Interesting morphologies like nano-ribbon for copper-phthalocyanine [96], nanoflowers for nickel phthalocyanine and zinc phthalocyanine [62] and nanowire for cobalt phthalocyanine [97] have been reported. Here, several factors such as nucleation, molecular diffusion, growth and anisotropic intermolecular interactions play an important role [98]. Phthalocyanines are known to transform from a meta-stable phase to a stable crystalline phase upon annealing [99]. Such polymorphs of phthalocyanines exhibit different optical and optoelectronic properties [100]. Similarly, phthalocyanine mixtures are also said to manifest physical properties different from pristine ones. Opitz et al. reported a blend of hydrogenated and fluorinated copper phthalocyanines deposited through co-evaporation where the reduced charge mobility in the blend suggests to be used as a charge generation

layer in tandem solar cells [101]. A decrease in resistance in thin films of mixed phthalocyanine deposited through a simultaneous thermal evaporation technique is reported [102]. There has been a recent focus on electroluminescence (EL) and photoluminescence properties of the metallo-phthalocyanine molecules [65,66,103,104]. Zinc phthalocyanine showed a dual emission tuned by its crystallinity upon excitation of 685 nm [69]. Here the alpha phase of ZnPc films showed excimer emission (930 nm) whereas the emission (780 nm) in the beta phase is attributed to the Frenkel exciton emission. Dendritic copper phthalocyanine soluble in DMF was synthesized that showed an aggregation-induced emission (AIE) around 480 nm [105]. Here the reaction time of water-aided aggregation played an important role in the determination of the solubility, molecular structures, crystallinity, thermal stability and solid-state fluorescent properties. The mechanisms corresponding to these luminescent properties are extracted through the excited states of phthalocyanine in their solid phases. Photoluminescence (PL) proves to be a powerful probe to study the excited states by assessing its properties, such as spectra, quantum yields, decay time, and temperature dependence [77]. It also provides a means to estimate the emission coefficients and yields of EL behaviour in materials [106].

Here we report our investigations on the Langmuir-Blodgett (LB) films of $CuPcOC_8$, $ZnPcOC_8$, and their mixture (1:1) which are characterized using Grazing incidence X-ray diffraction, atomic force microscopy, UV-visible spectroscopy, and photoluminescence spectroscopy techniques. In particular, we address how annealing improves crystallinity, formation of new phases, and enhances the emission properties. Surface manometry studies were carried out on $CuPcOC_8$ and $ZnPcOC_8$ at the air-water interface. Figure 9 shows the surface pressure – area per molecule (π-A_m) isotherms of $CuPcOC_8$ and $ZnPcOC_8$ at 293 K. The lift-off area for $CuPcOC_8$ is found to be 120 $Å^2$/molecule. Using the macrocycle of size 225 $Å^2$, and the projected area per molecule of $CuPcOC_8$ as 120 $Å^2$, the tilt angle is estimated to be 45˚ which agrees well with the reported value [107]. We find that the lift-off area of $ZnPcOC_8$ Langmuir monolayer to be around 220 $Å^2$/molecule. In literature, we find varying reports on the tilt angle for $ZnPcOC_8$ estimated through π-A_m isotherm. Burgués et al. have reported the lift-off area to be 140 $Å^2$/molecule which corresponds to the tilt angle of $ZnPcOC_8$ to be 36º [108]. Qiu et al. have reported the lift-off area of $ZnPcOC_8$ to be 160 $Å^2$/molecule which corresponds to the tilt angle of around 30º [48]. Considering the macrocycle of size 230 $Å^2$ and the projected area per molecule of $ZnPcOC_8$ to be 220 $Å^2$, our studies indicate that the $ZnPcOC_8$ lies face-on at the A-W interface. Further compression leads to a gradual increase in the surface pressure and the limiting area per molecule is found

to be 120 $Å^2$/molecule and 220 $Å^2$/molecule, for $CuPcOC_8$ and $ZnPcOC_8$ respectively. The mixture solutions of $CuPcOC_8$ and $ZnPcOC_8$ (0.9:1, 0.7:0.3, 0.6:0.4, 1:1) showed a decrease in the lift-off areas (220, 210, 200 and 175 $Å^2$/molecule, respectively).

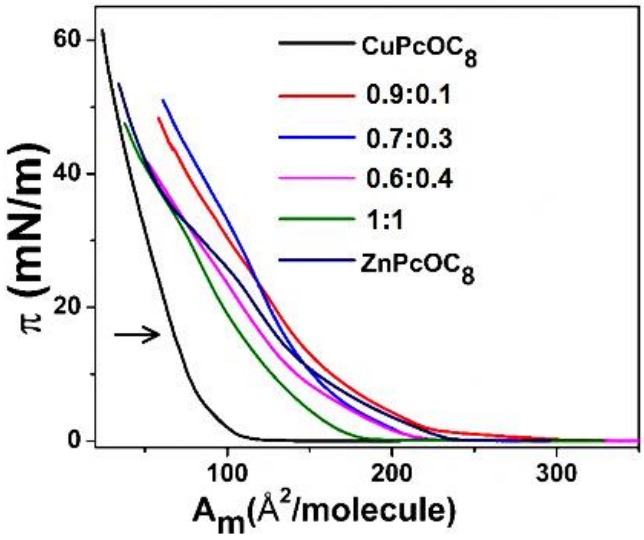

Figure 9: Surface pressure – Area per molecule (π-A_m) isotherm (293 K) of $CuPcOC_8$, $ZnPcOC_8$ and their mixtures at the air-water interface. Arrow mark shows the target pressure at which the Langmuir-Blodgett deposition was performed.

Figure 10a shows the GIXD pattern of LB film of $CuPcOC_8$. For the case of as-deposited and annealed (323 K) film of $CuPcOC_8$, a Bragg peak appears at 3.4° (inter-planar spacing, d = 25.9 Å). At 373 K, an additional Bragg peak appears at 3.5° (d = 24.9 Å) suggesting coexisting polymorphs. Annealing at 423 K and 473 K (in the liquid crystalline phase), further shifts the Bragg peak from 3.6° (d = 24.5 Å) to 3.8° (d = 23.2 Å). The powder X-ray diffraction data of $CuPcOC_8$ was analysed and the crystal structure was found to be monoclinic in nature (a = 34.72 Å, b = 7.86 Å, c = 26.09 Å, α = 90°, β = 100.6° and γ = 90°). The Bragg peak occurring at 3.6° (at 423 K) can be assigned to the (100) plane of the $CuPcOC_8$. Though the as-deposited film of $ZnPcOC_8$ did not exhibit Bragg peak, annealing the film at higher temperatures results in the improvement of crystallinity (Figure 10b). Annealing at 323 K results in a Bragg peak at 3.4° (d = 25.9 Å). At higher temperature (373 K), this results in an additional Bragg peak at 3.5° (d = 24.9 Å) is seen. Annealing at 373 K (in the liquid crystalline phase) shifts the Bragg peak to 3.5° (d = 24.9 Å). At 473 K, the Bragg peak is further shifted to 3.6° (d = 24.5 Å). Incidentally, $ZnPcOC_8$ also exhibits a columnar mesophase at 408 K and the differential scanning calorimetry studies on such systems report a solid to solid transition [109]. The powder X-ray diffraction pattern of the

$ZnPcOC_8$ was analyzed and found to belong to monoclinic crystal system (a = 23.80 Å, b = 5.84 Å, c = 20.57 Å, α = 90°, β = 95.9° and γ = 90°). The Bragg peak occurring at 3.6° (at 473 K) can be assigned to the (100) plane of the $ZnPcOC_8$. These studies show clear

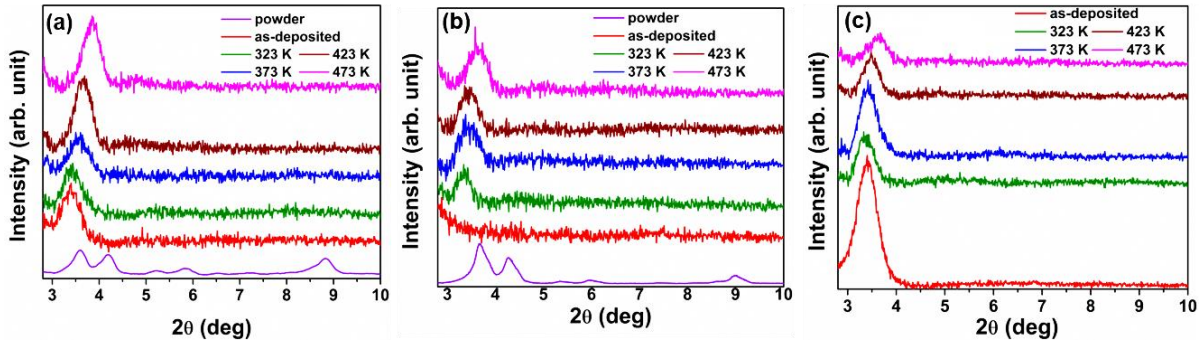

Figure 10: Grazing incidence X-ray diffraction patterns of LB films of (a) $CuPcOC_8$, (b) $ZnPcOC_8$, and (c) $CuPcOC_8/ZnPcOC_8$(1:1) mixture obtained at different annealing temperatures. The powder XRD patterns of $CuPcOC_8$ and $ZnPcOC_8$ is also shown for comparison.

evidence for structural changes in the annealed films of $CuPcOC_8$ and $ZnPcOC_8$ and yield support for the presence of different crystalline forms. Saini et al. have reported a Bragg peak at 3.5° (d = 25.6 Å) and 4.2° (d = 21.1 Å) for $CuPcOC_8$ and $ZnPcOC_8$ systems which were drop-casted onto glass substrate [110]. Our studies on thin films of $CuPcOC_8$ and $ZnPcOC_8$ yield rich features which are quite different from these reports. The GIXD pattern for the mixture (1:1) is presented in Figure 10c. The as-deposited film exhibits a Bragg peak at 3.4° (d = 25.9 Å) which persists with annealing (up to 373 K). Here too, annealing in liquid crystalline phase (beyond 373 K) tends to shift the Bragg peak to higher angle (3.6°, d = 24.5 Å).

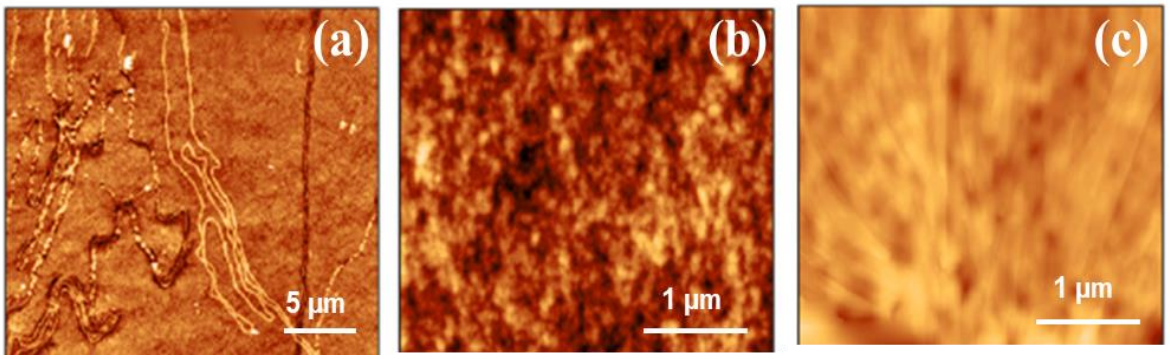

Figure 11: Surface topography images of LB films of (a) $CuPcOC_8$ (b) $ZnPcOC_8$ and (c) the mixture (1:1) at 293 K (as-deposited).

Figure 11 shows the surface topography of the as-deposited LB films of $CuPcOC_8$,

$ZnPcOC_8$ and their mixture (1:1). Interestingly, we find nanowire like structures for the as-deposited (Figure 11a) and the films annealed at 323 K. The dimensions of the nanowire are estimated to be 150 nm in width, extending up to 50 μm and is less dense. The nanowires were found to be stable at higher annealing temperatures (> 373 K). By following the surface topography changes with annealing temperature for $CuPcOC_8$ films, we infer the formation of new thin film polymorphs and their coexistence which agrees well with our GIXD results. The surface topography of the as-deposited $ZnPcOC_8$ LB films shows grainy texture (Figure 11b). For this case, GIXD studies reveal the absence of Bragg peak. Annealing at 323 K yields granular morphology. This is accompanied by the appearance of a Bragg peak at 3.4°. At an annealing temperature of 373 K, the granular structures are found to coexist with elongated needle-like features. Incidentally, at this temperature, we have observed an additional Bragg peak (3.5°) which can be attributed to the coexistence of polymorphs. At higher annealing temperatures (> 373 K) granular morphology is observed which is accompanied by a Bragg peak at 3.6°. These studies on $ZnPcOC_8$ highlight the influence of annealing on the surface topography and structural changes in the new thin film polymorphs. The surface topography of the mixture in thin-film form is quite different from that of the individual films. The as-deposited (Figure 11c) as well as the annealed films (323 K and 373 K) of the mixture exhibit both granular and needle-like morphologies. Based on AFM and GIXD studies (Bragg peak at 3.4°), we suggest solid-solid phase separation in the mixture. At higher annealing temperatures (423 K and 473 K), the needle-like morphology disappears and granular structures form. At these temperatures, the GIXD studies show a Bragg peak at a higher angle (3.6°). This shows that annealing from the liquid crystalline phase (423 K and 473 K), promotes new crystalline phase.

The UV-visible absorbance studies on the annealed LB films (quartz substrate) of $CuPcOC_8$, $ZnPcOC_8$ and their mixture, $CuPcOC_8/ZnPcOC_8$ (1:1) show the signatures of Q bands (about 680 nm and 710 nm, respectively) and B bands (around 280 nm and 300 nm, respectively) representing $\pi - \pi^*$ transitions of the electron from the ground state to the first ($S_0 \rightarrow S_1$) and second ($S_0 \rightarrow S_2$) excited state, respectively. For the case of LB films, we observe a red-shift in the absorbance of $CuPcOC_8$, $ZnPcOC_8$ and their mixture compared to that of respective solution spectra. This can be attributed to the exciton coupling effects due to the formation of J-aggregates in $CuPcOC_8$ and $ZnPcOC_8$, respectively [111].

The photoluminescence spectra obtained at an excitation of 300 nm for the as-deposited and annealed LB films of $CuPcOC_8$ is shown in Figure 12a. Deconvolution of this

spectra resulted in the peaks around 350, 380, 430 and 500 nm. Further, the ratio of the intensities around 500 nm and 380 nm is found to depend strongly on the annealing temperatures possibly indicating the change in the relative fraction of polymorphs

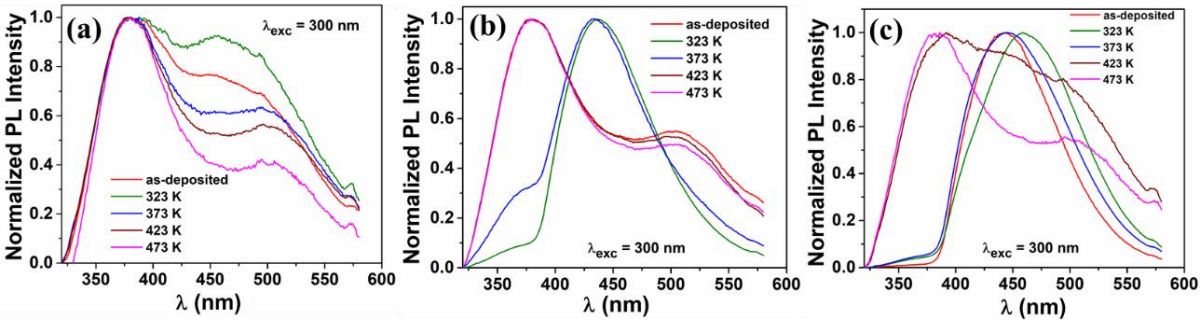

Figure 12: (a) Normalized photoluminescence spectra of as-deposited (293 K) and annealed LB films of (a) $CuPcOC_8$ (b) $ZnPcOC_8$ and (c) the mixture (1:1) at an excitation wavelength of 300 nm.

(Figure 12a). These studies reveal that the PL spectra obtained in the aggregated state (J-aggregates) largely differ from the solution form (monomeric). The surface topography of the thin film of $CuPcOC_8$ annealed at 323 K exhibiting nanowire feature transforms to the coexistence of thin crystalline flakes and nanowires at 373 K. Further, the GIXD pattern shows clearly a shift of the Bragg peak from 3.4° to 3.5° for the as-deposited and annealed film (< 373 K). For the films annealed beyond this temperature (373 K), the Bragg peak shifts to a higher angle (3.8°). Further, the PL studies reveal that the intensity ratio of the peak wavelengths around 350, 380 and 500 nm with respect to 430 nm showed an increasing trend beyond 323 K possibly indicating the change in the relative fraction of polymorphs (Figure 13a). Based on the GIXD, AFM and photoluminescence studies on thin films of $CuPcOC_8$, we infer the presence of different thin film polymorphs (Form-I and Form-II, below 373 K and Form-III, above 373 K).

For the case of $ZnPcOC_8$ film, a clear distinction in photoluminescence behavior is seen with annealing temperature (Figure 12b). For the as-deposited and annealed films (> 373 K) of $ZnPcOC_8$, deconvolution of these spectra resulted in the peaks around 350, 380, 415 and 500 nm. Interesting photophysical behavior is seen for the films annealed below 373 K. At 323 K and 373 K, in addition to 350, 415 and 500 nm, new emissions in the blue region (~ 400 nm and 450 nm) were observed. Noticeably the intensity ratio of the emission peaks around 350 and 500 nm with respect to 415 nm showed a considerable decreasing trend at 323 K and 373 K (Figure 13b). Interestingly, at these temperatures, GIXD and AFM studies show that

the additional Bragg peak appearing at 3.5° is accompanied by needle-like morphology which

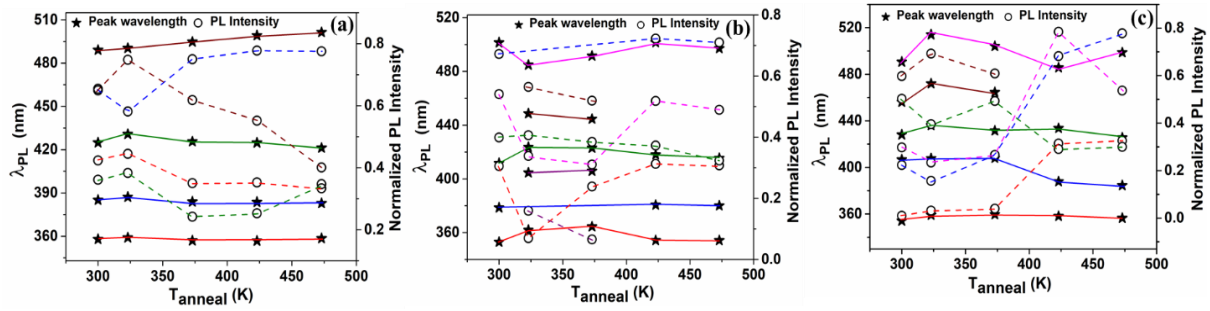

result in unique emission features. It may be noted that the GIXD and AFM studies of the as-

Figure 13: Variation of peak wavelength and photoluminescence intensity with annealing temperature (T_{anneal}) of the as-deposited (293 K) and annealed LB films of (a) $CuPcOC_8$ (b) $ZnPcOC_8$ and (c) the mixture (1:1) at an excitation wavelength of 300 nm.

deposited thin film of $ZnPcOC_8$ show the absence of Bragg peak and possess grainy texture whereas the film annealed above 373 K shows the presence of Bragg peak with granular morphology. From these results, we infer the presence of coexisting polymorphs (Form-I and Form-II) at 323 K and 373 K. Though the spectral features for the as-deposited and annealed films (> 373 K) were quite similar, GIXD and AFM results seem to suggest amorphous phase and Form-III polymorph. These studies highlight the intimate coupling between the structure and morphology of the thin film polymorphs dictating its property.

In the case of the $CuPcOC_8/ZnPcOC_8$ mixture (1:1), the deconvolution of the PL spectra for the films annealed below 373 K, resulted in the emission peaks around 350, 400, 430, 450 and 500 nm (Figure 12c). In contrast, for the films annealed above 373 K, the emission peak at 450 nm is absent. Negligible changes were observed in the peak wavelength (excluding 400 and 500 nm) of these deconvoluted emission peaks with the annealing temperature. The intensity ratio of the emission peaks around 350, 400 and 500 nm with respect to 430 nm also showed a drastic increase beyond 373 K (Figure 13c). The as-deposited and the films annealed up to 373 K showed an occurrence of new emission around 450 nm which is absent in the films annealed beyond 373 K. For this mixture, GIXD studies show a Bragg peak at 3.4° (Figure 10c). Further, the surface topographies show a coexisting granular and needle-like morphology for the films annealed up to 373 K. At higher temperatures (> 373 K), the GIXD studies show a Bragg peak at a higher angle (3.6º) with granular surface topography. The new emission observed around 450 nm for the annealed films (up to 373 K) also compliments these GIXD and AFM results. From these studies, we suggest that the films phase separate below an annealing temperature of 373 K for the mixture. Above 373 K, the

presence of granular morphology for the mixture suggests the miscibility of $CuPcOC_8$ and $ZnPcOC_8$ to a new crystalline phase. Based on the GIXD, AFM and photoluminescence studies we infer that the LB films of $CuPcOC_8$ and $ZnPcOC_8$ exhibit polymorphic nature and their mixture (1:1) tend to phase separate below 373 K.

Chapter 6: Summary and future scope

This section provides a comprehensive overview of the research work described in above chapters with their potential applications and the future scope.

Bibliography

[1] M. Fahlman, S. Fabiano, V. Gueskine, D. Simon, M. Berggren, X. Crispin, Interfaces in organic electronics, Nat Rev Mater. 4 (2019) 627–650.

[2] A. Sugimoto, H. Ochi, S. Fujimura, A. Yoshida, T. Miyadera, M. Tsuchida, Flexible OLED displays using plastic substrates, IEEE Journal on Selected Topics in Quantum Electronics. 10 (2004) 107–114.

[3] D.H. Kim, A. D'Aléo, X.K. Chen, A.D.S. Sandanayaka, D. Yao, L. Zhao, T. Komino, E. Zaborova, G. Canard, Y. Tsuchiya, E. Choi, J.W. Wu, F. Fages, J.L. Brédas, J.C. Ribierre, C. Adachi, High-efficiency electroluminescence and amplified spontaneous emission from a thermally activated delayed fluorescent near-infrared emitter, Nat Photonics. 12 (2018) 98–104.

[4] M. Wright, A. Uddin, Organic-inorganic hybrid solar cells: A comparative review, Solar Energy Materials and Solar Cells. 107 (2012) 87–111.

[5] Y. Xu, C. Liu, D. Khim, Y.Y. Noh, Development of high-performance printed organic field-effect transistors and integrated circuits, Physical Chemistry Chemical Physics. 17 (2015) 26553–26574.

[6] A. Brillante, I. Bilotti, R.G. Della Valle, E. Venuti, A. Girlando, Probing polymorphs of organic semiconductors by lattice phonon Raman microscopy, CrystEngComm. 10 (2008) 937–946.

[7] S. Riera-Galindo, A. Tamayo, M. Mas-Torrent, Role of Polymorphism and Thin-Film Morphology in Organic Semiconductors Processed by Solution Shearing, ACS Omega. 3 (2018) 2329–2339 .

[8] O.D. Jurchescu, D.A. Mourey, S. Subramanian, S.R. Parkin, B.M. Vogel, J.E.

Anthony, T.N. Jackson, D.J. Gundlach, Effects of polymorphism on charge transport in organic semiconductors, Phys Rev B Condens Matter Mater Phys. 80 (2009) 085201.

[9] S.T. Salammal, J.Y. Balandier, J.B. Arlin, Y. Olivier, V. Lemaur, L. Wang, D. Beljonne, J. Cornil, A.R. Kennedy, Y.H. Geerts, B. Chattopadhyay, Polymorphism in bulk and thin films: The curious case of dithiophene-DPP(Boc)-dithiophene, Journal of Physical Chemistry C. 118 (2014) 657–669.

[10] C.C. Mattheus, A.B. Dros, J. Baas, A. Meetsma, J.L. De Boer, T.T.M. Palstra, Polymorphism in pentacene, Acta Crystallographica Section C: Crystal Structure Communications. 57 (2001) 939–941.

[11] R.B. Campbell, J.M. Robertson, J. Trotter, The crystal and molecular structure of pentacene, Acta Crystallographica. 14 (1961) 705–711.

[12] H.L. Cheng, Y.S. Mai, W.Y. Chou, L.R. Chang, X.W. Liang, Thickness-dependent structural evolutions and growth models in relation to carrier transport properties in polycrystalline pentacene thin films, Adv Funct Mater. 17 (2007) 3639–3649.

[13] A.M. Hiszpanski, R.M. Baur, B. Kim, N.J. Tremblay, C. Nuckolls, A.R. Woll, Y.L. Loo, Tuning polymorphism and orientation in organic semiconductor thin films via post-deposition processing, Journal of the American Chemical Society. 136 (2014) 15749–15756.

[14] D. Käfer, L. Ruppel, G. Witte, Growth of pentacene on clean and modified gold surfaces, Physical Review B - Condensed Matter and Materials Physics. 75 (2007) 085309.

[15] N. Koch, A. Gerlach, S. Duhm, H. Glowatzki, G. Heimel, A. Vollmer, Y. Sakamoto, T. Suzuki, J. Zegenhagen, J.P. Rabe, F. Schreiber, Adsorption-induced intramolecular dipole: Correlating molecular conformation and interface electronic structure, Journal of the American Chemical Society. 130 (2008) 7300–7304.

[16] G. Bavdek, A. Cossaro, D. Cvetko, C. Africh, C. Blasetti, F. Esch, A. Morgante, L. Floreano, Pentacene nanorails on Au(110), Langmuir. 24 (2008) 767–772.

[17] G. Giri, E. Verploegen, S.C.B. Mannsfeld, S. Atahan-Evrenk, D.H. Kim, S.Y. Lee, H.A. Becerril, A. Aspuru-Guzik, M.F. Toney, Z. Bao, Tuning charge transport in solution-sheared organic semiconductors using lattice strain, Nature. 480 (2011) 504–508.

[18] L. Huang, Q. Liao, Q. Shi, H. Fu, J. Ma, J. Yao, Rubrene micro-crystals from solution routes: Their crystallography, morphology and optical properties, Journal of Materials Chemistry. 20 (2010) 159–166.

[19] S. Bergantin, M. Moret, Rubrene polymorphs and derivatives: The effect of chemical modification on the crystal structure, Crystal Growth and Design. 12 (2012) 6035–6041.

[20] H. Najafov, B. Lee, Q. Zhou, L.C. Feldman, V. Podzorov, Observation of long-range exciton diffusion in highly ordered organic semiconductors, Nature Materials. 9 (2010) 938–943.

[21] X. Wang, T. Garcia, S. Monaco, B. Schatschneider, N. Marom, Effect of crystal packing on the excitonic properties of rubrene polymorphs, CrystEngComm.18 (2016) 7353–7362.

[22] D.H. Arias, J.L. Ryerson, J.D. Cook, N.H. Damrauer, J.C. Johnson, Polymorphism influences singlet fission rates in tetracene thin films, Chem Sci. 7 (2016) 1185–1191.

[23] N.T. Boileau, R. Cranston, B. Mirka, O.A. Melville, B.H. Lessard, Metal phthalocyanine organic thin-film transistors: Changes in electrical performance and stability in response to temperature and environment, RSC Adv. 9 (2019) 21478–21485.

[24] C.G. Claessens, U. Hahn, T. Torres, Phthalocyanines: From outstanding electronic properties to emerging applications, Chemical Record. 8 (2008) 75–97.

[25] M. Gsänger, D. Bialas, L. Huang, M. Stolte, F. Würthner, Organic Semiconductors based on Dyes and Color Pigments, Advanced Materials. 28 (2016) 3615–3645.

[26] X. Li, E.Y. Park, Y. Kang, N. Kwon, M. Yang, S. Lee, W.J. Kim, C. Kim, J. Yoon, Supramolecular Phthalocyanine Assemblies for Improved Photoacoustic Imaging and Photothermal Therapy, Angewandte Chemie - International Edition. 59 (2020) 8630–8634.

[27] A.B. Sorokin, Phthalocyanine metal complexes in catalysis, Chem Rev. 113 (2013) 8152–8191.

[28] S. Yang, Y. Yu, X. Gao, Z. Zhang, F. Wang, Recent advances in electrocatalysis with phthalocyanines, Chem Soc Rev. 50 (2021) 12985–13011.

[29] K.M. Kadish, K.M. Smith, R. Guilard, The Porphyrin Handbook: Phthalocyanines: Properties and Materials, Elsevier 2012.

[30] D. Placencia, W. Wang, J. Gantz, J.L. Jenkins, N.R. Armstrong, Highly photoactive titanyl phthalocyanine polymorphs as textured donor layers in organic solar cells, Journal of Physical Chemistry C. 115 (2011) 18873–18884.

[31] T. Zou, X. Wang, H. Ju, Q. Wu, T. Guo, W. Wu, H. Wang, Crystal structure tuning in organic nanomaterials for fast response and high sensitivity visible-NIR photo-detector, J Mater Chem C Mater. 6 (2018) 1495–1503.

[32] V.M. Kaganer, H. Möhwald, P. Dutta, Structure and phase transitions in Langmuir monolayers, Rev Mod Phys. 71 (1999) 779–819.

[33] D. Hönig, D. Möbius, Direct visualization of monolayers at the air-water interface by Brewster angle microscopy, Journal of Physical Chemistry. 95 (1991) 4590–4592.

[34] H. Chung, Y. Diao, Polymorphism as an emerging design strategy for high performance organic electronics, Journal of Materials Chemistry C. 4 (2016) 3915–3933.

[35] M. Kothe, F. Widdascheck, G. Witte, Titanylphthalocyanine Films on Ag(111): An Epitaxial Metal/Organic Heterosystem with an Exceptional Smooth Surface, Journal of Physical Chemistry C. 123 (2019) 6097–6106.

[36] G. Zhang, B.L. Weeks, M. Holtz, Application of dynamic scaling to the surface properties of organic thin films: Energetic materials, Surf Sci. 605 (2011) 463–467.

[37] F. Biscarini, P. Samorí, O. Greco, R. Zamboni, Scaling behavior of anisotropic organic thin films grown in high vacuum, Phys Rev Lett. 78 (1997) 2389–2392.

[38] A.C. Dürr, F. Schreiber, K.A. Ritley, V. Kruppa, J. Krug, H. Dosch, B. Struth, Rapid Roughening in Thin Film Growth of an Organic Semiconductor (Diindenoperylene), Phys Rev Lett. 90 (2003) 4.

[39] S. Zorba, Y. Shapir, Y. Gao, Fractal-mound growth of pentacene thin films, Phys Rev B Condens Matter Mater Phys. 74 (2006) 245410 .

[40] S. Karan, B. Mallik, Power spectral density analysis and photoconducting behavior in copper(ii) phthalocyanine nanostructured thin films, Physical Chemistry Chemical Physics. 10 (2008) 6751–6761.

[41] S. Yim, T.S. Jones, Anomalous scaling behavior and surface roughening in molecular thin-film deposition, Phys Rev B Condens Matter Mater Phys. 73 (2006) 161305.

[42] S.M. Obaidulla, P.K. Giri, Surface roughening and scaling behavior of vacuum-deposited SnCl2Pc organic thin films on different substrates, Appl Phys Lett. 107 (2015) 221910.

[43] S. Chiodini, A. Straub, S. Donati, C. Albonetti, F. Borgatti, P. Stoliar, M. Murgia, F. Biscarini, Morphological Transitions in Organic Ultrathin Film Growth Imaged by in Situ Step-by-Step Atomic Force Microscopy, Journal of Physical Chemistry C. 124 (2020) 14030–14042.

[44] Ş. Ţălu, S. Stach, A. Mahajan, D. Pathak, T. Wagner, A. Kumar, R.K. Bedi, M. Ţălu, Multifractal characterization of water soluble copper phthalocyanine based films surfaces, Electronic Materials Letters. 10 (2014) 719–730.

[45] J. Kim, N. Lim, C.R. Park, S. Yim, Growth dynamics of ZnPc and TiOPc thin films: Effect of crystallinity on anomalous scaling behavior, Surf Sci. 604 (2010) 1143–1147.

[46] X. Zhang, E. Barrena, D. Goswami, D.G. De Oteyza, C. Weis, H. Dosch, Evidence for a layer-dependent ehrlich-schwöbel barrier in organic thin film growth, Phys Rev Lett. 103 (2009) 136101 .

[47] X.H. Li, M. Li, Z.H. Mai, Kinetic roughening of the interfaces of Langmuir-Blodgett films, Phys Rev B Condens Matter Mater Phys. 69 (2004) 235407.

[48] Y. Qiu, P. Chen, M. Liu, Interfacial assembly of an achiral zinc phthalocyanine at the air/water interface: A surface pressure dependent aggregation and supramolecular chirality, Langmuir. 24 (2008) 7200–7207.

[49] N.Q. Luc, V.S. Dang, H.H. Nguyen, A.T. Mai, Micro-rod single-crystalline phthalocyanine for photodetector development, Mater Sci Semicond Process. 125 (2021) 105638.

[50] H. Ren, J. De Chen, Y.Q. Li, J.X. Tang, Recent Progress in Organic Photodetectors and their Applications, Advanced Science. 8 (2021) 2002418.

[51] C. Wang, X. Chen, F. Chen, J. Shao, Organic photodetectors based on copper phthalocyanine films prepared by a multiple drop casting method, Org Electron. 66 (2019) 183–187.

[52] O.A. Melville, B.H. Lessard, T.P. Bender, Phthalocyanine-Based Organic Thin-Film Transistors: A Review of Recent Advances, ACS Appl Mater Interfaces. 7 (2015) 13105–13118.

[53] C.R. Newman, C.D. Frisbie, D.A. Da Silva Filho, J.L. Brédas, P.C. Ewbank, K.R. Mann, Introduction to organic thin film transistors and design of n-channel organic semiconductors, Chemistry of Materials. 16 (2004) 4436–4451.

[54] O. Ostroverkhova, Organic Optoelectronic Materials: Mechanisms and Applications, Chem Rev. 116 (2016) 13279–13412. https://doi.org/10.1021/acs.chemrev.6b00127.

[55] M. Urbani, M.E. Ragoussi, M.K. Nazeeruddin, T. Torres, Phthalocyanines for dye-sensitized solar cells, Coord Chem Rev. 381 (2019) 1–64.

[56] J. Yang, D. Yan, T.S. Jones, Molecular Template Growth and Its Applications in Organic Electronics and Optoelectronics, Chem Rev. 115 (2015) 5570–5603.

[57] S.M. Bayliss, S. Heutz, R. Cloots, R.L. Middleton, G. Rumbles, T.S. Jones, Templating effects in the growth of metal-free phthalocyanine polymorphic double layers, Advanced Materials. 12 (2000) 202–206.

[58] S. Nešpůrek, H. Podlesak, C. Hamann, Structure and photoelectrical behaviour of

vacuum-evaporated metal-free phthalocyanine films, Thin Solid Films. 249 (1994) 230–235.

[59] R.D. Gould, Structure and electrical conduction properties of phthalocyanine thin films, Coord Chem Rev. 156 (1996) 237–274.

[60] S.M. Bayliss, S. Heutz, G. Rumbles, T.S. Jones, Thin film properties and surface morphology of metal free phthalocyanine films grown by organic molecular beam deposition, Physical Chemistry Chemical Physics. 1 (1999) 3673–3676.

[61] S. Dalgleish, L. Reissig, Y. Shuku, C. Gourlaouen, S. Vela, K. Awaga, Controlling the crystallinity and crystalline orientation of “shuttlecock” naphthalocyanine films for near-infrared optoelectronic applications, J Mater Chem C Mater. 6 (2018) 1959–1970.

[62] S. Karan, B. Mallik, Nanoflowers grown from phthalocyanine seeds: Organic nanorectifiers, Journal of Physical Chemistry C. 112 (2008) 2436–2447.

[63] H. Lim, S. Yang, S.H. Lee, J.Y. Lee, Y. Lee, A.B. Situmorang, Y.H. Kim, J.W. Kim, Influence of the metal phthalocyanine molecular orientation on charge separation at the organic donor/acceptor interface, J Mater Chem C Mater. 9 (2021) 2156–2164.

[64] N. Rawat, Z. Pan, L.W. Manning, C.J. Lamarche, I. Cour, R.L. Headrick, R. Waterman, A.R. Woll, M.I. Furis, Macroscopic Molecular Ordering and Exciton Delocalization in Crystalline Phthalocyanine Thin Films, Journal of Physical Chemistry Letters. 6 (2015) 1834–1840.

[65] E. Zysman-Colman, S.S. Ghosh, G. Xie, S. Varghese, M. Chowdhury, N. Sharma, D.B. Cordes, A.M.Z. Slawin, I.D.W. Samuel, Solution-Processable Silicon Phthalocyanines in Electroluminescent and Photovoltaic Devices, ACS Appl Mater Interfaces. 8 (2016) 9247–9253.

[66] A.R. Gómez, C.M. Sánchez-Hernández, I. Fleitman-Levin, J. Arenas-Alatorre, J.C. Alonso-Huitrón, M.E.S. Vergara, Optical absorption and visible photoluminescence from thin films of silicon phthalocyanine derivatives, Materials. 6 (2014) 6585–6603.

[67] E. Yabaş, E. Biçer, R. Katırcı, Experimental and In Silico studies on optical properties of new thiadiazole tetrasubstituted metal-free and zinc phthalocyanine compounds, Opt Mater (Amst). 122 (2021).

[68] G.L. Pakhomov, D.M. Gaponova, A.Y. Luk’yanov, E.S. Leonov, Luminescence of phthalocyanine thin films, Physics of the Solid State, 47, (2005) 170–173.

[69] S. Hammer, T. Ferschke, G. V. Eyb, J. Pflaum, Phase transition induced spectral tuning of dual luminescent crystalline zinc-phthalocyanine thin films and OLEDs, Appl Phys Lett. 115 (2019) 263303 .

[70] M. Urbani, G. De La Torre, M.K. Nazeeruddin, T. Torres, Phthalocyanines and

porphyrinoid analogues as hole-and electron-transporting materials for perovskite solar cells, Chem Soc Rev. 48 (2019) 2738-2766 .

[71] C. Bizzarri, E. Spuling, D.M. Knoll, D. Volz, S. Bräse, Sustainable metal complexes for organic light-emitting diodes (OLEDs), Coord Chem Rev. 373 (2018) 49-82 .

[72] I. Nar, A. Atsay, H. Pekbelgin Karaoğlu, A. Altındal, E. Hamuryudan, π-Extended hexadeca-substituted cobalt phthalocyanine as an active layer for organic field-effect transistors, Dalton Transactions. 47 (2018) 15017-15023 .

[73] P. Nayak, P. Viswanath, UV photodetector based on self-affine Langmuir-Blodgett film of nickel octabutoxy phthalocyanine doped with stearic acid, Opt Mater (Amst). 122 (2021) 111807 .

[74] T.C. Gunaratne, A. V. Gusev, X. Peng, A. Rosa, G. Ricciardi, E.J. Baerends, C. Rizzoli, M.E. Kenney, M.A.J. Rodgers, Photophysics of octabutoxy phthalocyaninato-Ni(II) in toluene: Ultrafast experiments and DFT/TDDFT studies, Journal of Physical Chemistry A. 109 (2005) 2078–2089.

[75] S. Heutz, S.M. Bayliss, R.L. Middleton, G. Rumbles, T.S. Jones, Polymorphism in phthalocyanine thin films: Mechanism of the α → β transition, Journal of Physical Chemistry B. 104 (2000) 7124–7129.

[76] S. Karan, B. Mallik, Effects of annealing on the morphology and optical property of copper (II) phthalocyanine nanostructured thin films, Solid State Commun. 143 (2007) 289-294.

[77] Y. Sakakibara, R.N. Bera, T. Mizutani, K. Ishida, M. Tokumoto, T. Tani, Photoluminescence properties of magnesium, chloroaluminum, bromoaluminum, and metal-free phthalocyanine solid films, Journal of Physical Chemistry B. 105 (2001) 1547–1553.

[78] A. Sarkar, K.A. Suresh, Negative differential resistance in nickel octabutoxy phthalocyanine and nickel octabutoxy phthalocyanine/graphene oxide ultrathin films, J Appl Phys. 123 (2018) 155501 .

[79] W.Y. Tong, H.Y. Chen, A.B. Djurišić, A.M.C. Ng, H. Wang, S. Gwo, W.K. Chan, Infrared photoluminescence from α- and β-copper phthalocyanine nanostructures, Opt Mater (Amst). 32 (2010) 924–927.

[80] Y. Kaneko, Y. Nishimura, N. Takane, T. Arai, H. Sakuragi, N. Kobayashi, D. Matsunaga, C. Pac, K. Tokumaru, Violet emission observed from phthalocyanines, J Photochem Photobiol A Chem. 106 (1997) 177–183.

[81] W. Bała, M. Wojdyła, M. Rebarz, M. Szybowic, M. Drozdowski, A. Grodzicki, P. Piszczek, Influence of central metal atom in MPc (M = Cu, Zn, Mg, Co) on Raman,

FT-IR, absorbance, reflectance, and photoluminescence spectra, Journal of Optoelectronics and Advanced Materials. 11 (2009) 264–269.

[82] A.A. Zanfolim, D. Volpati, C.A. Olivati, A.E. Job, C.J.L. Constantino, Structural and electric-optical properties of zinc phthalocyanine evaporated thin films: Temperature and thickness effects, Journal of Physical Chemistry C. 114 (2010) 12290–12299.

[83] Z.T. Liu, H.S. Kwok, A.B. Djurišić, The optical functions of metal phthalocyanines, J Phys D Appl Phys. 37 (2004) 678–688.

[84] B.R. Hollebone, M.J. Stillman, Assignment of absorption and magnetic circular dichroism spectra of solid, α phase metallophthalocyanines, Journal of the Chemical Society, Faraday Transactions 2: Molecular and Chemical Physics. 74 (1978) 2107–2127.

[85] Optical Properties of Copper Phthalocyanine(CuPc)Thin Films, Egyptian Journal of Solids. 24 (2001) 11-19 .

[86] M. Wojdyła, B. Derkowska, Z. Łukasiak, W. Bała, Absorption and photoreflectance spectroscopy of zinc phthalocyanine (ZnPc) thin films grown by thermal evaporation, Mater Lett. 60 (2006) 3441-3446 .

[87] M. Wojdyła, W. Bała, B. Derkowska, M. Rebarz, A. Korcala, The temperature dependence of photoluminescence and absorption spectra of vacuum-sublimed magnesium phthalocyanine thin films, Opt Mater (Amst). 30 (2008) 734-739 .

[88] A.B. Djurišić, T. Fritz, K. Leo, Modeling the optical constants of organic thin films: Application to 3,4,9,10-perylenetetracarboxylic dianhydride (PTCDA), Opt Commun. 183 (2000) 123–132.

[89] H. Fujiwara, Spectroscopic Ellipsometry: Principles and Applications, 2007. https://doi.org/10.1002/9780470060193.

[90] A.B. Djurišić, C.Y. Kwong, T.W. Lau, W.L. Guo, E.H. Li, Z.T. Liu, H.S. Kwok, L.S.M. Lam, W.K. Chan, Optical properties of copper phthalocyanine, Opt Commun. 205 (2002) 155–162.

[91] M.A. Barrett, Z. Borkowska, M.W. Humphreys, R. Parsons, Ellipsometry of thin films of copper phthalocyanine, Thin Solid Films. 28 (1975) 289-302 .

[92] G.E. Jellison, Data analysis for spectroscopic ellipsometry, Thin Solid Films. 234 (1993) 416–422.

[93] A. Franke, A. Stendal, O. Stenzel, C. Von Borczyskowski, Gaussian quadrature approach to the calculation of the optical constants in the vicinity of inhomogeneously broadened absorption lines, Pure and Applied Optics 5 (1996) 845–853.

[94] B.R. Kaafarani, Discotic liquid crystals for opto-electronic applications, Chemistry of Materials. 23 (2011) 378–396.

[95] W. Huang, J. Yu, X. Yu, Y. Li, H. Zeng, Performance enhancement of organic thin-film transistors with improved copper phthalocyanine crystallization by inserting ultrathin pentacene buffer, Thin Solid Films. 520 (2012) 6677–6680.

[96] F. Liu, J. Sun, S. Xiao, W. Huang, S. Tao, Y. Zhang, Y. Gao, J. Yang, Controllable fabrication of copper phthalocyanine nanostructure crystals, Nanotechnology. 26 (2015) 225601.

[97] X. Ji, T. Zou, H. Gong, Q. Wu, Z. Qiao, W. Wu, H. Wang, Cobalt phthalocyanine nanowires: Growth, crystal structure, and optical properties, Crystal Research and Technology. 51 (2016) 154–159.

[98] F. Ghani, H. Gojzewski, H. Riegler, Nucleation and growth of copper phthalocyanine aggregates deposited from solution on planar surfaces, Applied Surface Science. 351 (2015) 969–976.

[99] S. Harish T, P. Viswanath, Annealing assisted structural and surface morphological changes in Langmuir-Blodgett films of nickel octabutoxy phthalocyanine, Thin Solid Films. 598 (2016) 170–176.

[100] D. Roy, N.M. Das, N. Shakti, P.S. Gupta, Comparative study of optical, structural and electrical properties of zinc phthalocyanine Langmuir-Blodgett thin film on annealing, RSC Advances. 4 (2014) 42514–42522.

[101] A. Opitz, B. Ecker, J. Wagner, A. Hinderhofer, F. Schreiber, J. Manara, J. Pflaum, W. Brütting, Mixed crystalline films of co-evaporated hydrogen- and fluorine-terminated phthalocyanines and their application in photovoltaic devices, Organic Electronics. 10 (2009) 1259–1267.

[102] A.C. Varghese, C.S. Menon, Electrical conductivity studies of mixed phthalocyanine thin films, Central European Journal of Physics. 3 (2005) 8–14.

[103] A.K. Pal, S. Varghese, D.B. Cordes, A.M.Z. Slawin, I.D.W. Samuel, E. Zysman-Colman, Near-Infrared Fluorescence of Silicon Phthalocyanine Carboxylate Esters, Scientific Reports. 7 (2017) 12282 .

[104] M. Alkhamisi, V. V. Korolkov, A.S. Nizovtsev, J. Kerfoot, T. Taniguchi, K. Watanabe, N.A. Besley, E. Besley, P.H. Beton, The growth and fluorescence of phthalocyanine monolayers, thin films and multilayers on hexagonal boron nitride, Chemical Communications. 54 (2018) 12021–12024.

[105] J. Wang, L. Pan, X. Zhou, K. Jia, X. Liu, Dendritic copper phthalocyanine with aggregation induced blue emission and solid-state fluorescence, Chemical Physics

Letters. 660 (2016) 143–148.

[106] Z. Fan, C. Cheng, S. Yu, K. Ye, R. Sheng, D. Xia, C. Ma, X. Wang, Y. Chang, G. Du, Red and near-infrared electroluminescence from organic light-emitting devices based on a soluble substituted metal-free phthalocyanine, Optical Materials. 31 (2009) 889–894.

[107] A. Biadasz, B. Bursa, B. Barszcz, A. Bogucki, B. Laskowska, A. Graja, D. Wróbel, Thermodynamics and in-situ absorption of Langmuir monolayers of selected copper phthalocyanine substituted with different peripheral groups, Dyes and Pigments. 89 (2011) 86–92.

[108] J. Torrent-Burgués, P. Cea, I. Giner, E. Guaus, Characterization of Langmuir and Langmuir-Blodgett films of an octasubstituted zinc phthalocyanine, Thin Solid Films. 556 (2014) 485–494.

[109] J. Sleven, T. Cardinaels, C. Görller-Walrand, K. Binnemans, Liquid-crystalline metallophthalocyanines containing late first-rowtransition metals, ARKIVOC 2003 (iv) 68-82.

[110] R. Saini, A. Mahajan, R.K. Bedi, D.K. Aswal, A.K. Debnath, Phthalocyanine based nanowires and nanoflowers as highly sensitive room temperature Cl2 sensors, RSC Advances. 4 (2014) 15945–15951.

[111] T. V. Basova, M. Çamur, A.A. Esenpinar, S. Tuncel, A. Hassan, A. Alexeyev, H. Banimuslem, M. Durmu, A.G. Gürek, V. Ahsen, Effect of substituents on the orientation of octasubstituted copper(II) phthalocyanine thin films, Synthetic Metals. 162 (2012) 735–742.